SOFT ROBOTS

Bioinspired photoresponsive soft robotic lens

Corey Zheng[1,2] and Shu Jia[1,2,3]*

Vision is a critical sensory function for humans, animals, and engineered systems, enabling environmental perception essential for imaging and autonomous operation. Although bioinspired, tunable optical systems have advanced adaptability and performance, challenges remain in achieving biocompatibility, robust yet flexible construction, and specialized multifunctionality. Here, we present a photoresponsive hydrogel soft lens (PHySL) that combines optical tunability, an all-solid configuration, and high resolution. PHySL leverages a dynamic hydrogel actuator that autonomously harnesses optical energy, enabling substantial focal tuning through all-optical control. Beyond mimicking biological vision, the system achieves advanced functionalities, including focus control, wavefront engineering, and optical steering by responding to spatiotemporal light stimuli. PHySL highlights the potential of optically powered soft robotics applied in soft vision systems, autonomous soft robots, adaptive medical devices, and next-generation wearable systems.

INTRODUCTION

Living organisms have evolved into highly sophisticated systems capable of performing dynamic feats, including complex navigation, nimble flight, and self-sustenance. Consequently, their forms and functions have long served as inspiration for artificial designs, ranging from behavior-based algorithms and animal-inspired kinematics to soft robotics using materials with tissue-like compliance (*1*–*8*). Central to the capabilities of animals are complex sensory systems that enable them to effectively perceive and interpret their surroundings. Vision, in particular, stands out as one of the most critical senses, and adaptation to various ecological niches has yielded a remarkable array of biological optical architectures. Animal eyes reflexively respond to changing environmental conditions and combine robust, soft, lightweight, and compact designs with functionalities including improved light efficiency (*9*), panoramic vision (*10*), aberration-based chromatic vision (*11*), specialized pupil deformations (*12*), and adjustable focus (*13*).

These features have prompted substantial efforts in bioinspired optics, aiming to replicate the advantages of biological eyes to meet growing demands across robotics (*14*–*16*), mobile devices (*17*, *18*), medical and health tools (*19*–*22*), biological imaging (*23*–*25*), and environmental surveillance (*26*), among others. For example, the compound-eye structure of insects has led to the development of artificial vision systems with ultrawide fields of view (FOVs) (*27*). Moth-inspired photonic architectures have been adopted as a basis for antireflective coatings (*28*). The elongated pupils of felines have informed hardware-based camouflage-breaking techniques (*29*). Notably, the camera eye, shared by humans, vertebrates, and several invertebrates, can dynamically modify its focal length by altering lens curvature (*30*), and this ability has inspired a variety of tunable lens designs (*31*, *32*). For example, fluid-based approaches can manipulate liquid volume, modify the curvature of a fluid meniscus or encapsulating membrane, and change the focal length (*33*–*45*). All-solid tunable optics similarly mimic the camera eye by deforming a central polymer lens with radial actuators, analogous to natural accommodation (*46*). These systems can be driven by conventional mechanical actuators, including an array of motors or mechanical irises (*47*, *48*) or soft muscle–like dielectric elastomer actuators (*49*–*54*).

Despite these advances, current camera eye–style tunable optics still face several challenges that limit their capabilities for supporting autonomy and vision in diverse, unstructured environments akin to those encountered in nature. Prominently, natural eyes are highly capable in these environments owing to their focal tuning capabilities, a soft and robust structure, and capacity for advanced optical adaptations, all of which are achieved in a self-powered organism. In many cases, tunable lenses require electronic power sources and control signals, which may not be practical in energy-limited or flexible systems incompatible with rigid electronics. Likewise, fluid-based methods are vulnerable to mechanical shock and require proper sealing (*55*). Motorized solid tunable lenses use rigid actuators, reducing compactness and flexibility, whereas dielectric elastomer actuator devices are inherently soft but require high driving voltages (>1 kV for millimeter-scale thicknesses) (*56*–*58*), complicating power demands. In contrast, biological eyes combine tunability, robustness, and flexibility in a self-sustaining organism powered by energy harnessed from the environment.

Hydrogels, with their biocompatible nature and tissue-like softness, hold substantial promise for soft vision systems. They have already been used in biocompatible optical applications such as hydrogel optical fibers and commercial contact lenses (*59*–*62*). Furthermore, they are multifunctional materials that can combine both actuation and sensing into a single platform, achieving an automatic response to external stimuli while harvesting energy from their surroundings (*63*–*66*). They are thus widely used in soft robotics, where they function as actuators, sensors, and wearable interfaces (*67*, *68*). Current stimulus-responsive hydrogel tunable optics designs have considerable room for growth. Although focal tuning has been demonstrated (*41*, *42*, *69*), they are generally overshadowed by other powerful tunable optics technologies. Leveraging the soft and continuum actuation capabilities of these materials could yield biomimetic capabilities combining all-solid and soft biocompatible construction, untethered or passive operation, and advanced optical capabilities.

Here, we present the bioinspired photoresponsive hydrogel soft lens (PHySL) that achieves optical tunability and an all-solid configuration with resolution and focal modulation comparable to the human eye. We developed a soft device fabrication process, realizing an integrated high-quality elastomer optic and hydrogel

[1]Laboratory for Systems Biophotonics, Georgia Institute of Technology, Atlanta, GA 30332, USA. [2]Wallace H. Coulter Department of Biomedical Engineering, Georgia Institute of Technology and Emory University, Atlanta, GA 30332, USA. [3]Parker H. Petit Institute for Bioengineering and Biosciences, Georgia Institute of Technology, Atlanta, GA 30332, USA.
*Corresponding author. Email: shu.jia@gatech.edu

actuator system. PHySL leverages a photoresponsive hydrogel as a continuum actuator that autonomously responds to incoming light, stably deforming a central lens via radial stretching. This mechanism harnesses optical energy directly from the environment, driving substantial focal variations through all-optical control. PHySL exhibits high sensitivity to ambient lighting conditions, providing considerable freedom beyond previous soft tunable lenses for complex functionalities, including open-loop focus control, wavefront engineering, and optical steering in response to spatiotemporal illumination patterns. We further demonstrate the potential of PHySL by integrating it into a fiber-optic imager, multiplexing imaging and control, and developing a proof-of-concept electronics-free fluidic soft imager. Positioned at the intersection of soft robotics, materials, and optics, PHySL represents an advance toward enhancing flexible systems with visual capabilities, promising applications in autonomous soft robots, medical devices, wearable technologies, and beyond.

RESULTS

PHySL principle, fabrication, and mechanical characterization

Conventional tunable optics approaches often rely on electronic control schemes, fluidic interfaces, or rigid materials that require large footprints, thereby hindering their integration into a variety of soft systems (table S1). In this work, PHySL leverages responsive hydrogels to effectively combine optical control, energy harvesting, and robust all-soft construction, thus advancing the development of flexible, autonomous, and efficient vision systems. PHySL comprises a soft polydimethylsiloxane (PDMS) lens that is deformed by radial forces from a poly(*N*-isopropylacrylamide) (PNIPAM) hydrogel embedded with broadband light–absorbing reduced graphene oxide (rGO) (Fig. 1A). Under illumination, PHySL increases in focal length and pupil size, akin to human vision reflexes (*13*, *46*). The photothermal heating effect of rGO drives PNIPAM above its lower critical solution temperature (~32°C) (*70*), leading to a phase change that deswells the gel via expulsion of water from the gel and contraction of the gel matrix (*71*–*73*). As the gel shrinks, it applies radial tension to the central lens (Fig. 1B and fig. S1). This process flattens the lens via radial stretching and increases pupil size, extending the focal length in a process analogous to the human far-vision reflex in which the lens flattens to elongate focal length while the pupil concurrently dilates (*74*). Once the exposure ceases, the gel cools, returns to its original phase, and reswells, returning the system to its baseline state. Our device's pupil behavior is the inverse of the biological pupillary reflex, which would typically constrict the pupil in response to increased light without changing the lens curvature (*75*) (Supplementary Text). This design ensures superior mechanical stability, because the photoresponsive shrinkage of the gel actuator places the lens into tension, eliminating vulnerabilities to undesired lens buckling compared with compressive designs required for a normal pupillary reflex or with other hydrogel-based actuators using bending or buckling for motion (*76*).

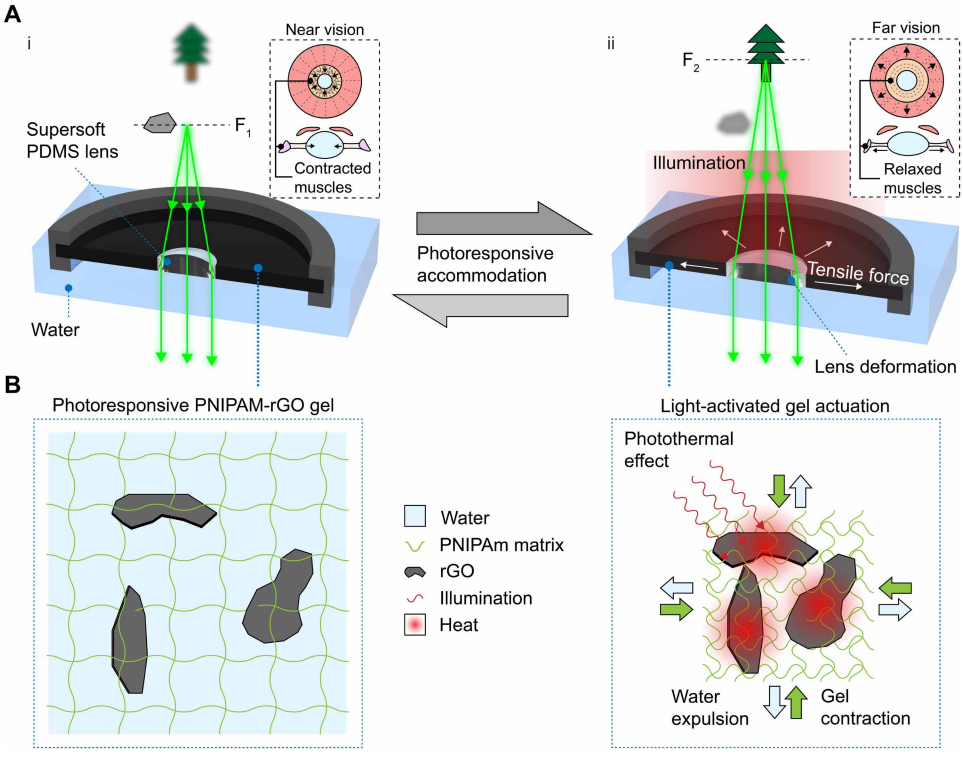

Fig. 1. Principle of PHySL. (**A**) PHySL transitions between near-focus (i) and far-focus (ii) states under exposure to an optical stimulus. Insets: Corresponding states of the biological counterpart, a human lens and pupil, under near-vision and far-vision conditions. (**B**) Structure of the baseline hydrated state of PNIPAM-rGO gel, corresponding to the near-vision state, and structure of the irradiated PNIPAM-rGO gel, exhibiting light-activated gel actuation, which manifests as gel deswelling.

To characterize the technique, we first measured its photoresponsive behavior, where we placed fully hydrated PNIPAM-GO and PNIPAM-rGO samples with a GO concentration of 2.5 mg/ml in a custom immersion chamber on a tensile testing machine (detailed in Materials and Methods). With both ends of each sample fixed, the gels were exposed to 350 mW/cm^2 of 850-nm near-infrared (NIR) illumination in air, revealing a notable two-step actuation process. Upon initial illumination, a rapid increase in tension was observed, peaking at ~73.0 kPa for PNIPAM-rGO and 52.0 kPa for PNIPAM-GO, consistent with the expected higher absorption efficiency of rGO (Fig. 2, A and B). Given that rGO is nearly uniformly absorbing across a broad light spectrum, the gel response was independent of the illumination wavelength (fig. S2). Once NIR was switched off (Fig. 2A, black tabs), the gels exhibited an immediate surge in force, reaching peak nominal stresses of 128.3 kPa for PNIPAM-rGO and 76.7 kPa for PNIPAM-GO within seconds. As the gel cooled, it gradually relaxed, overshooting its initial tension before returning close to the baseline only after reimmersion in water (Fig. 2A and movie S1). Notably, this second-stage increase in force after NIR removal has not been previously reported in PNIPAM-rGO/GO systems, suggesting that the incorporation of GO may unlock additional actuation pathways (Supplementary Text and fig. S3).

Next, we fabricated a soft, tissue-like PDMS lens via a specialized molding process (detailed in Materials and Methods). Considering the measured actuation capabilities of PNIPAM-rGO, we selected Sylgard 527 PDMS, which has a tissue-like modulus of elasticity as low as 5 kPa (*77*). This softness accommodates large deformations and reduces mechanical mismatch with biological tissues, typically characterized by stiffness below 100 kPa (*78*). We refined multiple Sylgard 527 mixtures and identified an optimal 1:1.3 base–to–cross-linker ratio, producing the lens with an elastic modulus of 9.5 kPa (Fig. 2C) and transparency > 90%. In practice, because soft materials are difficult to release from rigid templates, we used supersoft lithography (*79*). A hard template was created by shaping Sylgard 184 PDMS droplets into gravity-driven lens surfaces (*80*) and then transferring them onto a dissolvable mold. We cast Sylgard 527 PDMS into this mold and dissolved it afterward, allowing for easy demolding of the lens with minimal surface damage (Fig. 2D-i).

The PNIPAM-GO hydrogel containing GO (2.5 mg/ml) was robustly cross-linked to the lens using benzophenone treatment (*81*), forming a flexible yet strong interface that remained intact even under high strain (Fig. 2D-ii, fig. S4A, and Supplementary Text). Subsequently, the PNIPAM-GO hydrogel was chemically reduced to PNIPAM-rGO through hydrazine immersion, after which the entire device was then mounted (Fig. 2D-iii). The resulting hydrogel was highly absorptive over broad wavelengths, with a transmission of only ~0.7%. Here, we used a rigid 3D-printed mount for ease of integration with microscope components. However, it should be noted that PHySL does not inherently require rigid supports and can be readily adapted to soft elastomers to form a robust all-soft system capable of retaining the same optical performance even after sustaining stress and deformations (Mechanical durability in Supplementary Text, figs. S4B and S5, and movie S2). Detailed fabrication procedures are provided in Materials and Methods and fig. S6. With this design, PHySL can achieve more than 20% expansion of the lens diameter (movie S3).

Tunability and optical capabilities of PHySL

Next, we evaluated performance by incorporating PHySL into a standard bright-field microscope setup (Fig. 3A and fig. S7). The device was positioned in a shallow tray of water, ensuring that its upper surface was exposed to air. This arrangement increased the

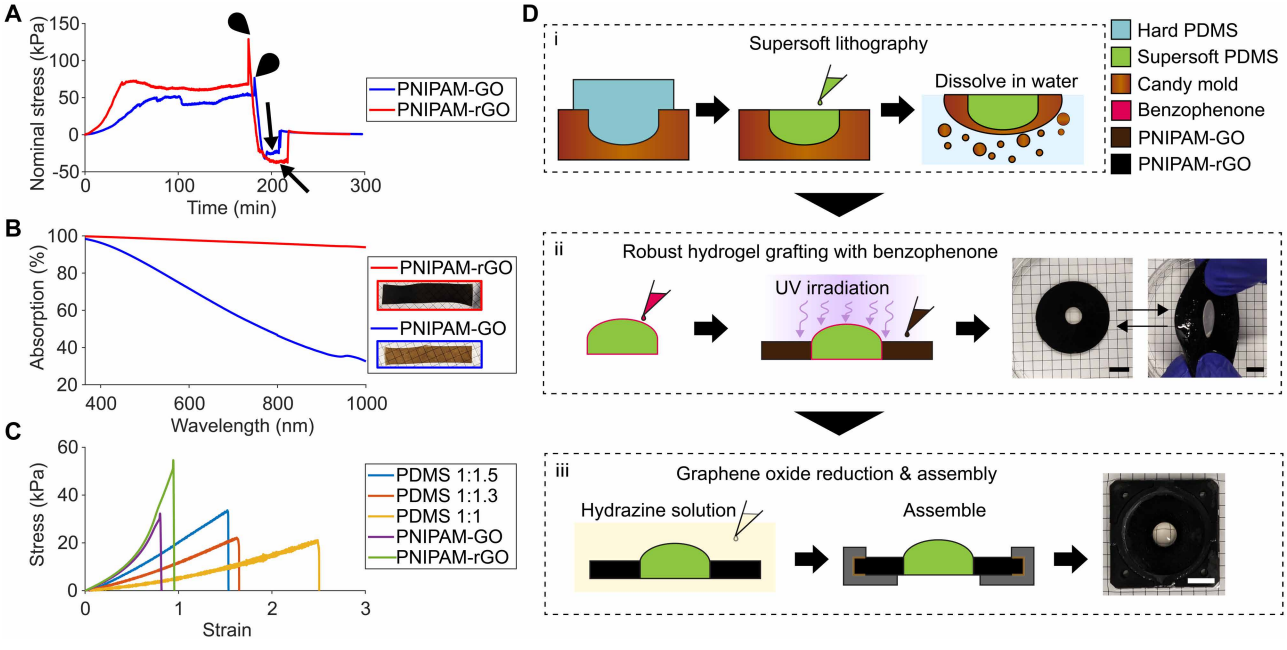

Fig. 2. Key mechanical characteristics and fabrication process of PHySL. (**A**) Nominal stress exerted by gels in response to NIR exposure. Black pointers indicate when NIR illumination was turned off. Black arrows indicate when additional water was added to the hydrogel chamber. (**B**) Absorptance of a 1-mm-thick hydrogel sample before and after reduction of GO. (**C**) Elastic curves for PNIPAM-GO, PNIPAM-rGO, and three supersoft PDMS recipes. (**D**) Three key steps toward PHySL fabrication: (i) supersoft lithography, (ii) robust hydrogel grafting, and (iii) device assembly. Scale bars, 10 μm.

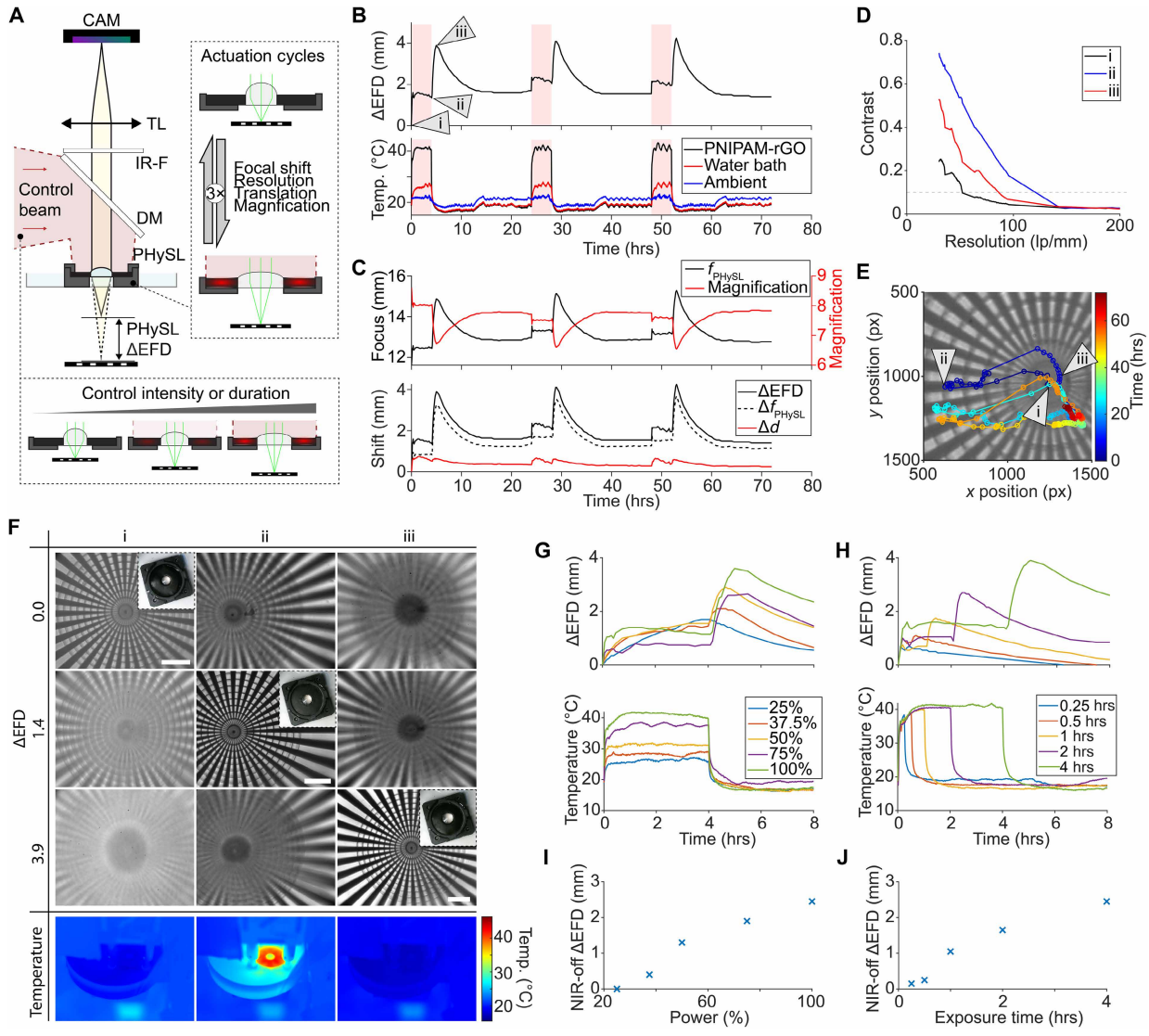

Fig. 3. Characterization of PHySL. (**A**) Schematic of the microscope setup that integrates PHySL. CAM, camera; TL, tube lens; IR-F, infrared filter; DM, dichroic mirror. Actuation cycles: A three-cycle on-off experiment determines the optical properties of PHySL. Control intensity or duration: PHySL's response to varying energies is determined. (**B**) Relative focal shift during three exemplary on-off NIR illumination cycles and the corresponding temperatures of the PHySL gel and environment. Transparent red zones indicate when NIR illumination is on. Pointers indicate selected experimental time points at the baseline state before illumination (i), after 4 hours of NIR exposure in the first cycle (ii), and at the maximum focal shift achieved during the first cycle (iii). hrs, hours. (**C**) PHySL's magnification and focal shift properties. Magnification calculated from in-focus images during the three-cycle PHySL actuation is overlaid with the calculated true focal length of PHySL. The corresponding overall focal shift (ΔEFD) is decomposed into contributions from axial translation of principal planes (Δd) and photoresponsive focal length shift (Δf_{PHySL}). (**D**) MTF of PHySL calculated on the basis of in-focus images at each time point specified in (B). The horizontal dashed line represents the 10% contrast limit, which was used as the resolvability limit in this work. (**E**) Tracking of lateral image motion during the three-cycle PHySL actuation. Pointers indicate the central locations of the Siemens star at the corresponding time points specified in (B), showing the lateral motion in one on-off cycle and its similarity to subsequent cycles. (**F**) Image snapshots extracted from three depths at each time point specified in (B), identifying varying focal planes with ΔEFD values of 0.0 mm (i), 1.4 mm (ii), and 3.9 mm (iii), along with a thermal image corresponding to each time point. (**G**) Focal shifts in PHySL in response to five levels of illumination intensity and the corresponding gel temperatures. (**H**) Focal shifts in PHySL in response to five levels of illumination duration at 100% intensity and the corresponding gel temperatures. (**I** and **J**) Maximum focal shift achieved after turning off NIR illumination versus illumination power (I) and the maximum focal shift achieved after turning off NIR illumination versus illumination duration (J). All scale bars, 200 μm.

refractive power of the system and facilitated water reabsorption into the gel. An 850-nm light-emitting diode (LED) provided radially isotropic illumination across the lens, with irradiance ranging from ~260 mW/cm^2 at the center to 150 mW/cm^2 at the periphery. The photoresponsive properties of PHySL were initially characterized by repeated optical stimulation cycles. In practice, the lens underwent multiple 24-hour on-off cycles, each comprising 4 hours of irradiation at the maximum intensity, followed by 20 hours off. Distinct physical changes, including visual indications of gel phase transition and an increase in lens diameter, were observed in response to the stimulation (fig. S1). We measured the corresponding focusing ability of the lens by monitoring the effective focal distance (EFD), i.e., the distance between stimulus-induced focal planes from the reference, throughout each cycle. In the first 10 min

of illumination, the EFD increased by 11.6% (1.35 mm) of the baseline focal distance as the gel reached 40°C within 5 min (Fig. 3B). Notably, we observed the two-step EFD variation in line with the PNIPAM-rGO actuation dynamics (Fig. 2D), which exhibited the initial stage where under continued NIR exposure, the EFD peaked at 13.8% (1.6 mm) greater than the baseline after 20 min and then stabilized with only a minor 2.2% (0.25 mm) decrease. Subsequently, after switching off NIR, the EFD rose by an additional 21.9% (2.55 mm) over 50 min, obtaining a total change of 33.6% (3.9 mm) (movie S4). To ensure reliable performance, we then characterized the focal response for five sequential 1-hour illuminations, finding that the variability was less than 250 μm (<2%) across cycles (Supplementary Text and fig. S5).

We then evaluated the underlying mechanisms governing the observed change in EFD, ΔEFD, whose variations were primarily induced by two main factors, i.e., the focal change resulting from the photoresponsive deformation of the lens curvature ($\Delta f_{\mathrm{PHySL}}$) and the axial movement of the lens principal planes during deformation (Δd). With the 4f imaging system, we tracked system magnification to determine the focal length of PHySL (f_{PHySL}) and then decomposed ΔEFD into its two components (Fig. 3C and Materials and Methods). During the initial optical stimulation, the axial movement accounted for up to 46.9% of the EFD variation, whereas upon turning off the NIR light, it contributed only 13.4%. As a result, the maximal focal length change due solely to the photoresponsive deformation of lens curvature was about 3.3 mm or 29% of the baseline focal length of 11.6 mm, comparable to the accommodation of the human eye (~25%) (*46*, *82*). Notably, to evaluate imaging capacity during actuation, we calculated the associated modulation transfer function (MTF), revealing a resolution ranging between 50 and 120 line pairs (lp)/mm, comparable to that of the human eye (*83*), and enhanced lens transparency as the photoresponsive temperature increased (Fig. 3D and fig. S8). Furthermore, PHySL exhibited cyclical lateral translation, demonstrating repeatable actuation that can be further optimized through an improved fabrication process or environmental control (Fig. 3E). Moreover, minimal distortion was observed across different stages, indicating isotropic deformation in actuation cycles (Fig. 3F).

Furthermore, we characterized the responsiveness of PHySL with respect to ambient conditions, illumination duration, and power (movie S5). Governed by a photothermal process, the focus-changing behavior of PHySL also depends on the environmental temperature. We found that under elevated temperatures, the baseline focal length of PHySL increased but resulted in similar second-stage EFD shifts (fig. S9 and Supplementary Text). Furthermore, the recovery speed was slowed, indicating the reduced capability of PHySL to reabsorb water under elevated temperature. Testing PHySL's behavior in response to various illumination intensities, we found an increase in EFD variations with higher exposure times and intensities (Fig. 3, G and H). Specifically, at lower irradiances (~25% power; 37.5 to 65.0 mW/cm^2) or shorter durations (~15 min), a noticeable change in focal length occurred without the two-step actuation. At even lower light levels comparable to diffuse reflections from objects in a daylight scene (5 mW/cm^2), the focus was minimally changed, stabilizing at only a 200-μm increase or <2% more than the baseline focal length (fig. S9 and Supplementary Text). By contrast, higher exposures produced two-step actuation, and especially the second-stage EFD shift, triggered after turning off the illumination, was proportionally scaled with the total energy absorbed (Fig. 3, I and J). These results indicated that PHySL can harvest and store optical energy from its surrounding environment. Notably, although PHySL's total energy consumption was higher than some electronic tunable lens technologies (table S1), it could still be actuated at irradiances near 60 mW/cm^2, comparable to that of direct sunlight at Earth's surface (*84*–*86*), suggesting its potential usability under passive stimulation without needing photovoltaics or other components. Moreover, within the range of energy levels tested, no saturation of the focal shift was observed, which implies that the tuning range could be further extended.

Multiscale PHySL imaging of biological specimens and natural scenes

Using the same 4f microscope configuration, we first examined a range of biological specimens with PHySL (Fig. 4, A to F). In a *Dictydium* fungus sample, PHySL resolved two parallel fibers separated by ~5 μm (Fig. 4A). It also distinguished microscopic hairs on an ant leg at 9-μm spacing (Fig. 4B) and measured the 4-μm gap between the claws of a tick leg (Fig. 4C). Furthermore, to illustrate volumetric sectioning capabilities, we imaged three stacked microscope slides, containing ocean diatoms, paramecia, and various pollens, which formed a total thickness of 2.9 mm. Driving PHySL with NIR light, we conducted depth scans throughout the entire volume (Fig. 4D and movie S5). Notably, PHySL consistently captured fine details across its full tuning range (figs. S10 and S11), including the gap between a cell nucleus (Fig. 4E) and the lobes of a pollen grain (Fig. 4F).

Last, we evaluated PHySL as a single-lens imager under general-purpose conditions (Fig. 4G). This configuration yielded an FOV of ~30°. To drive PHySL, an angled NIR illumination source produced an irradiance of 140 to 230 mW/cm^2 from the lens edge to its center. PHySL sequentially scanned the full depth range, imaging objects located 7.5 to 203 cm away under ambient lighting (Fig. 4H and movie S6). For example, at 10 cm, PHySL resolved <200-μm gaps in a circuit connector, and at 50.5 cm, it distinguished converging lines on a playing card down to 2.0 mm (Fig. 4, I and J). Although the current images appear blurry, we can enhance the image quality through several strategies, including alternate lens materials, additional apertures, or different illumination schemes (Supplementary Text and fig. S12). In the single-lens configuration, we also tested PHySL's imaging capabilities when positioned at different orientations and found minimal variations in imaging performance even when inverted or held sideways (Supplementary Text and fig. S13). These results underscore the potential of PHySL for integration into vision systems for tunable imaging across multiple spatial scales and conditions.

Wavefront manipulation using spatiotemporally patterned illumination

Furthermore, we demonstrated extended degrees of optical manipulation in PHySL when subjected to patterned or sequenced illumination. Specifically, besides continuous scanning, we assessed the ability of the tunable lens to curate a desired focal set point with temporally modulated illumination. As shown, under an open-loop control scheme that adjusts illumination power and timing, PHySL maintained focus within 100 μm (2.5% of its maximum range) (Fig. 5A), stabilizing at the target for more than 2 hours and minimizing lateral motion (Fig. 5B and movie S7). Furthermore, we show that PHySL can be controlled in a feedback-based manner using an autofocus algorithm and even controlled in a remote-viewing

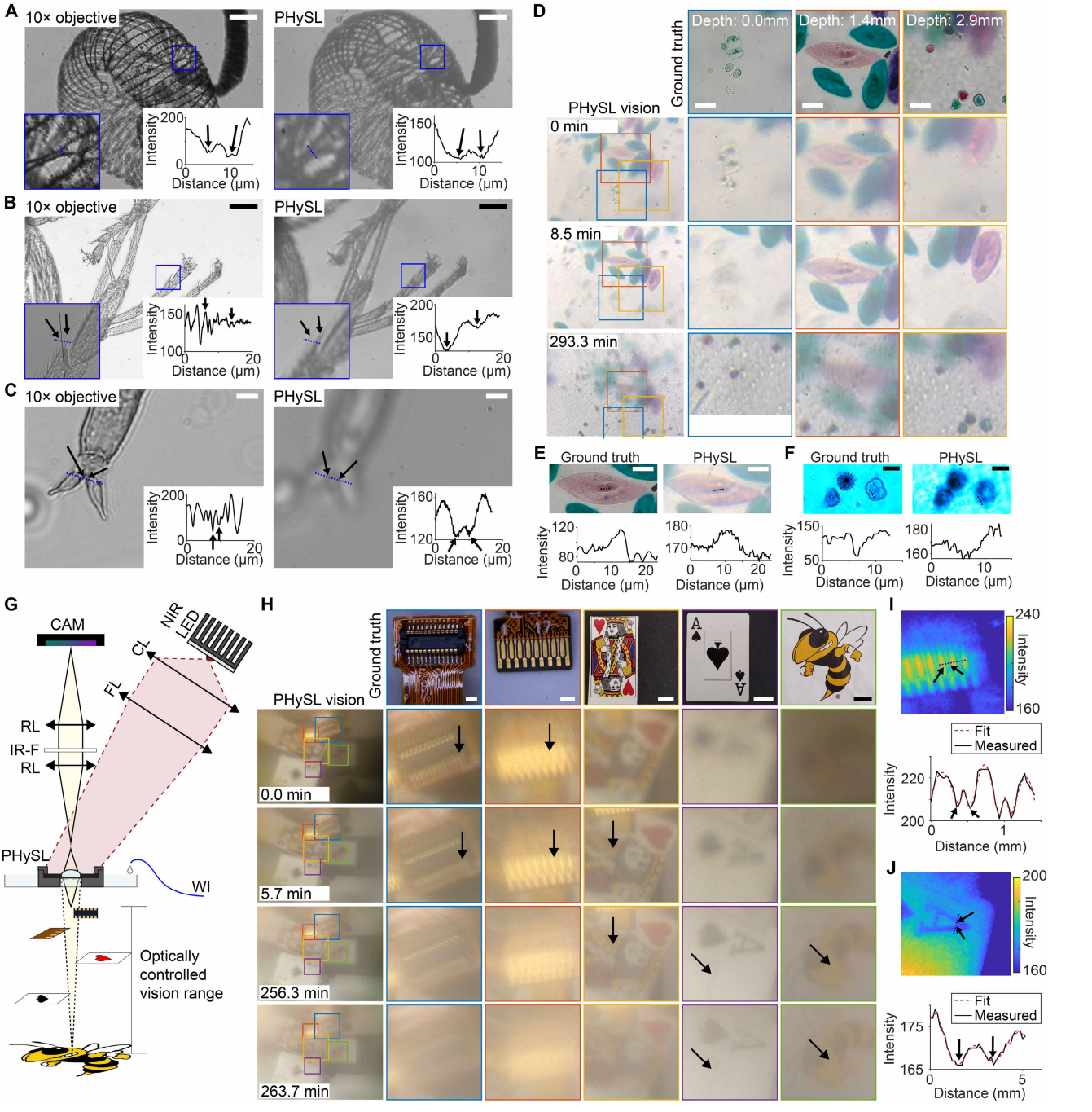

Fig. 4. Imaging biological samples and natural scenes with PHySL. (**A** to **C**) Comparing microscope objective– and PHySL-acquired single images. (A) Parallel fibers of a *Dictydium* fungus. Insets: Magnified views of the region in the blue box and intensity profile across the blue dashed line. Scale bars, 50 μm. (B) Ant leg hairs. Blue box inset: Close-up of hairs in blue box region. The image is divided into two depths (solid black line) to focus on two hairs in different planes (arrows). Graph inset: Intensity profile across the blue dashed line. (C) Tick claws. Inset: Intensity profile across the blue dashed lines, showing a gap in claws. (**D**) PHySL photoresponsive volumetric scan of a layered three-dimensional (3D) microscope sample in comparison with ground truth images at specific depths acquired using a 10× objective lens. (**E**) Comparison of ground truth and PHySL images across a gap feature in a paramecium nucleus. (**F**) Comparison of ground truth and PHySL images across a division in pollen grain lobes. For both images, only the blue color channel was used. (**G**) Single-lens PHySL imaging a room-scale scene. RL, relay lens; CL, condenser lens; FL, focusing lens; WI, water infusion. (**H**) Tunable focusing across several objects in ambient room lighting. Reference images are shown in the top row. From left to right, an integrated circuit chip, flex cable connector, king of hearts playing card, ace of spades playing card, and the Georgia Tech mascot Buzz were placed at varying distances from the imager. Arrows indicate features shifting in and out of focus during scanning. (**I**) PHySL image of the fine gaps in the flex cable terminals. The measured profile (black) and Gaussian-fitted profile (dotted red) resolved a separation distance of 160 μm (arrows). (**J**) PHySL image of the gap between converging lines in the character "A." The measured profile (black) and Gaussian-fitted profile (dotted red) resolved a separation of 2 mm (arrows). Scale bars, 50 μm [(A), (B), and (E)], 10 μm (C), 60 μm (D), and 25 μm (F). From left to right (H), 1, 1, 10, 20, and 40 mm.

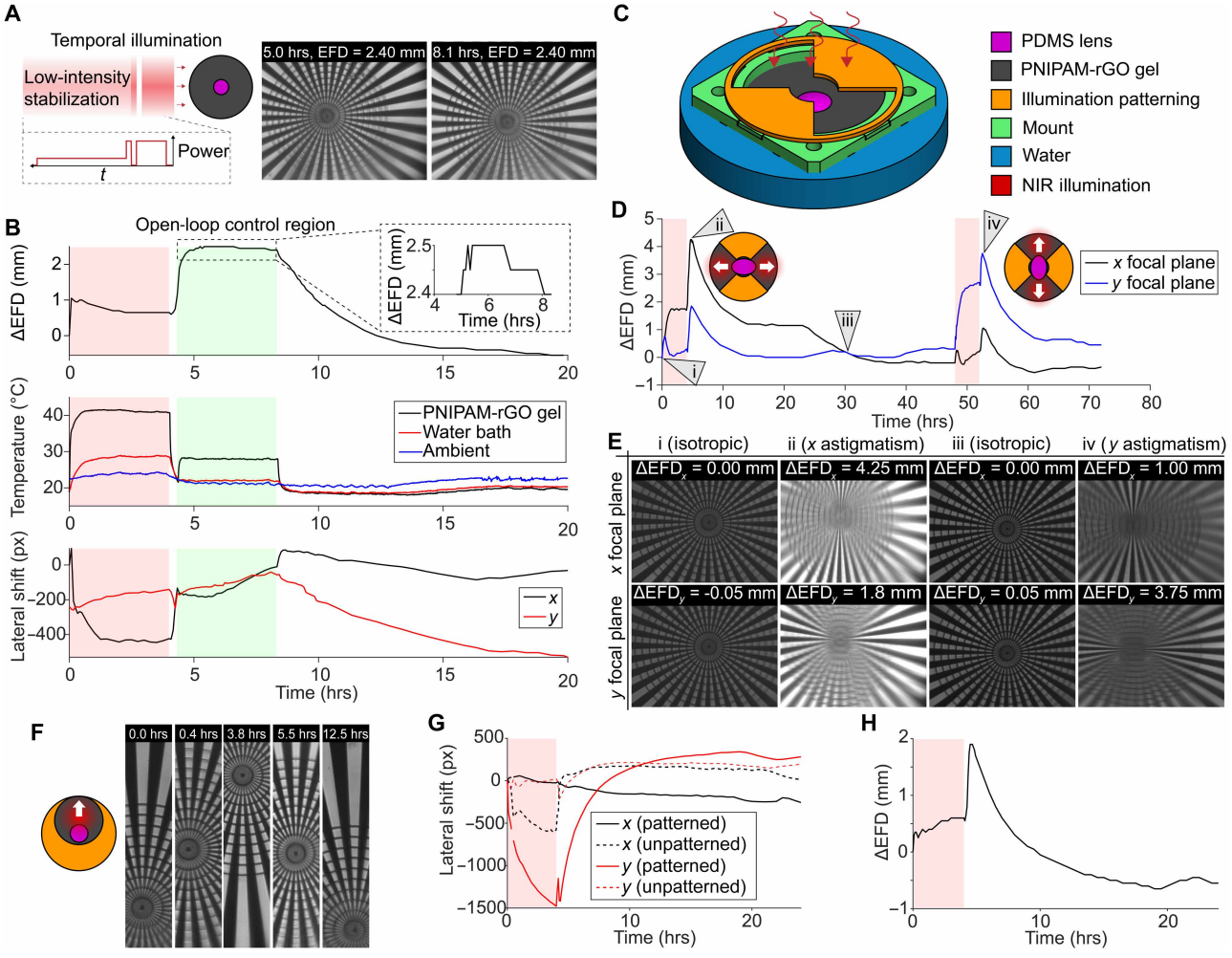

Fig. 5. Spatiotemporal patterned illumination control of PHySL to achieve versatile functions. (**A**) Temporal illumination modulation at different intensities generates a stable focus and lateral position even over hours. (**B**) Responses of PHySL during open-loop control, exhibiting the changes in EFD, gel and environmental temperatures, and lateral shift of the lens. The red zone indicates NIR illumination at full power, whereas the green zone indicates NIR illumination of 35% to maintain focus via open-loop control. Inset: Open-loop control region demonstrating stabilized focus within a 2.5% (100 μm) range for >2 hours. (**C**) Diagram of the astigmatic patterned illumination scheme consisting of a quadrant mask. (**D**) Measured ΔEFD of the *x* and *y* focal planes measured for orthogonal astigmatic patterned illuminations. Number labels indicate key time points extracted for visualization. Red zones indicate NIR illumination at full power. (**E**) Visualization of the *x* and *y* focal planes at each labeled time point in (D). (i) Initial state demonstrating isotropic visualization. (ii) Induced astigmatism from *x*-oriented patterned illumination, demonstrating a relatively increased ΔEFD along the *x* axis compared with the *y* axis. (iii) Recovery of the lens to an isotropic state. (iv) Induced astigmatism from *y*-oriented patterned illumination, demonstrating a relatively increased ΔEFD along the *y* axis compared with the *x* axis (**F**) Diagram of offset aperture illumination pattern with a time lapse of lateral translation during illumination (0 to 3.8 hours) followed by recovery in the opposite direction with no illumination (5.5 and 12.5 hours). (**G**) Comparison of lateral translation for actuations with offset illumination (patterned) and without patterned illumination, i.e., illuminating the entire PHySL surface (unpatterned). The red zone indicates NIR illumination at full power. (**H**) Overall measured change in EFD during translation. The red zone indicates NIR illumination at full power.

application through a fiber-optic image relay (Supplementary Text and fig. S14). Future refinements, such as calibrating open-loop responses or implementing closed-loop feedback, may enhance the controllability of these modes. Next, we used quadrant-patterned illumination, selectively activating opposing regions of the lens (Fig. 5C). By applying tension along a single axis, this scheme induced abnormal deformation and astigmatism corresponding to the chosen orthogonal orientations of illumination (Fig. 5D), achieving a maximum EFD difference of 2.7 mm between the *x* and *y* foci. Notably, PHySL recovered to an isotropic state in the absence of illumination (Fig. 5E and movie S8), showing the reversible nature of this astigmatic control. Last, we demonstrated controlled image translation with minimal distortion using an off-centered circular illumination pattern (Fig. 5F). Under these conditions, translation along the primary offset of illumination (i.e., the *y* axis) increased by more than threefold relative to uniform illumination, whereas displacement along the orthogonal dimension (i.e., the *x* axis) remained comparatively suppressed (Fig. 5G and movie S9). An overall focal shift was also observed (Fig. 5H). Collectively, these findings illustrate that the spatiotemporal control of illumination enables PHySL to exhibit a diverse array of lens functionalities. Integrating specialized control schemes or masks may further confer biomimetic attributes such as camouflage disruption or chromatic vision. As a dynamic and multifunctional lens, PHySL thus holds

promise for soft robotic vision systems requiring high-resolution imaging and versatile sensing capabilities.

DISCUSSION

Vision represents one of the most critical sensory functions for vertebrates, offering high imaging performance, tunability, robust yet flexible construction, and specialized adaptations. In this work, we reported a bioinspired PHySL. Notably, PHySL achieves a synergistic combination of functionalities that make it uniquely suitable for soft systems. We achieved robust, all-optical focal tunability (~30%) and high resolution (50 to 120 lp/mm), both comparable to those of the human eye. Simultaneously, PHySL exploits ambient stimuli of diverse spatiotemporal patterns to generate complex lensing effects and functionalities, such as open-loop focus control, wavefront engineering, and optical steering. The results validated PHySL in remote all-optical control and maneuverability, and we further demonstrated manipulation of PHySL under irradiances comparable to sunlight at Earth's surface, highlighting the energy harvesting capabilities of the device.

PHySL represents a promising approach in areas where traditional optics face limitations, including in soft robotics and medical devices. Optical control of the lens reduces reliance on electrical connections and complexity, suitable for remote imaging systems (Supplementary Text). Moreover, PHySL supports the development of vision sensors highly compatible with soft systems. By fusing photoresponsive microfluidic computation and PHySL, we created the prototype of an electronics-free fluidic imager (termed PHySL-EYE; Supplementary Text and fig. S15). Such a design holds potential for improved integration into soft robots, compatibility with alternative power or control schemes, and decreased reliance on rigid traditional imaging arrays. Thus, the versatile capabilities of PHySL, coupled with its potential to passively function untethered and battery-free, may lead to enhanced autonomy and sensing in soft systems across various settings by equipping them with compatible vision systems.

Prominently, PHySL opens multiple avenues for future development (Supplementary Text). For example, integrating additional optical components such as independent apertures and lensing components, changing lens materials, or modifying the design structure enables customization of the feedback behavior, focal length, imaging quality, and incident light (figs. S8 and S12). Incorporating advanced materials with improved response speed and mechanical strength could mitigate its relatively long actuation times and broaden its range of lens deformation (*87*–*91*). In addition, a key consideration is PHySL's operating environment. PHySL's environmental sensitivity may result in difficulty operating under fluctuating thermal conditions. Potentially, chemical modifications could be performed to better target specific temperature ranges (*92*) or compensated by active closed-loop schemes. Refined designs or alternative materials could further expand its applicability in various environments (figs. S8, S12, and S16) (*93*, *94*). Integration with flexible curved sensor arrays could yield biomimetic chambered eye designs, potentially encapsulating the system with an internal water reservoir and improving image quality and FOV in a single-lens design (Supplementary Methods and fig. S17). Moreover, ongoing advances in stretchable metaoptics, electronics, and fluidic circuitry (*95*–*105*) may enable further capabilities of soft vision systems. These could integrate PHySL for enhanced response complexity and environmental awareness, enabling image feedback capabilities in passively powered soft robotics. Positioned at the interface of soft robotics, functional materials, and optics, PHySL, therefore, offers opportunities for applications in autonomous, environment-aware vision systems.

MATERIALS AND METHODS

PHySL fabrication

Chemical preparation

A 50-ml stock of PNIPAM-GO solution was created by adding 15 ml of deionized (DI) water and 15 ml of GO [highly concentrated GO (5 g/liter), Graphene Supermarket] to a 50-ml centrifuge tube; 8.49 g of PNIPAM (415324, Sigma-Aldrich) was added, and the mixture was vortexed (Analog Vortex Mixer, VWR) for 10 s. Afterward, equal parts of DI water and GO were added until the mixture totaled 50 ml, resulting in a final PNIPAM concentration of 1.5 M. The mixture was vortexed again until the PNIPAM grains were completely dissolved. The stock solution was stored at room temperature. Before usage, the stock was ultrasonicated in a water bath (CPX1800, Fisherbrand) for 15 min to dissolve any precipitate.

The *N*,*N*′-methylenebisacrylamide (MBAA) stock solution was created by adding 0.1 g of MBAA (146072, Sigma-Aldrich) to 10 ml of water. The mixture was vortexed for 60 s to ensure complete dissolution of MBAA and then stored at 4°C. Before usage, the stock was vortexed for 10 s.

The benzophenone solution was created by adding reagent alcohol (12R1001, Decon Labs) to 1 g of benzophenone until the mixture volume totaled 10 ml. The mixture was vortexed until the benzophenone crystals completely dissolved.

Hanging droplet lens master mold

First, positive lens molds were created using the hanging droplet technique (*100*). An array of cylinders 8 mm in diameter and 2 mm in height was created by molding hard PDMS (Sylgard 184, Dow Silicone Corporation) in a 1:10 cross-linker–to–base ratio to a 3D-printed negative mold (Form 2, Formlabs) as shown in fig. S6A-i. The cylinders were used as the hanging platform, constraining the diameter of the PDMS lens to the diameter of the cylinder. Drops of Sylgard 184 PDMS in a 1:10 cross-linker–to–base ratio were deposited onto each cylinder via a syringe with a 25-gauge needle (fig. S6A-ii). The cylinder array was then inverted and positioned above a hot plate at 60°C for 24 hours to cure the PDMS lens (fig. S6A-iii), resulting in the positive lens mold. The positive lens mold was then fixed to the bottom of a 100-ml silicone beaker using additional Sylgard 184 PDMS (fig. S6A-iv) and cured for 4 hours at 120°C, resulting in the final master mold (fig. S6A-v).

Supersoft lithography

PHySL has a low modulus of <10 kPa and thus is difficult to peel from conventional molds without damage. Instead, a dissolvable sugar mold was created following a supersoft lithography process (*78*); 10 ml of light corn syrup (Karo) and 20 ml of table sugar (pure granulated sugar extra fine, Publix) were mixed thoroughly and then poured onto the positive lens mold (fig. S6B-i). The container was then sequentially microwaved (The Genius Sensor 1250W, Panasonic) and degassed in a vacuum desiccator (Bel-Art) for several cycles (fig. S6B-ii) to achieve a bubble-free negative dissolvable mold of the lens array (fig. S6B-iii,iv). The parameters of each cycle are listed in table S2.

Soft PDMS (Sylgard 527, Dow Silicone Corporation) was mixed in a 1:1.3 part A–to–part B ratio and then deposited into each lens

cavity using a syringe (fig. S6C-i). The entire mold was enclosed in a petri dish and heated at 50°C for 24 hours (fig. S6C-ii), after which it was allowed to cool to room temperature. Individual lenses were released by submerging the mold in water for 1 hour, dissolving the sugar (fig. S6C-iii). Lenses were rinsed with water and then methanol and blown dry with air. After cleaning, lenses were placed suspended from a metal platform and further cured at 120°C for another 24 hours (fig. S6C-iv).

PHySL assembly

The PNIPAM-GO stock solution was chilled in an ice bath while simultaneously bubbled with nitrogen gas for 5 min. Then, the hydrogel precursor solution was formed by combining 1 ml of PNIPAM-GO stock solution, 60 μl of MBAA stock, and 3 mg of potassium persulfate (216224, Sigma-Aldrich) in a 2-ml centrifuge tube. Nitrogen was gently blown into the top of the tube, which was quickly sealed, vortexed for 10 s, and then placed in an ice bath.

Next, the fabricated supersoft lens was prepared for hydrogel bonding. A benzophenone stock solution was poured into a plastic tray. The lens was immersed in the solution for 1 min (fig. S6D-i) and then removed. Afterward, the lens was cleaned three times by rinsing with methanol (MX0475, Supelco) and blown dry with nitrogen each time. The treated lens was placed on a clean silicon wafer inside a petri dish. A PDMS ring mold was then centered around the lens. The assembly was placed on top of a chilling platform consisting of a heat sink submerged in ice (fig. S6D-ii).

Five microliters of *N*,*N*,*N*′,*N*′-tetramethylethylenediamine (T9281, Sigma-Aldrich) was added to the previously prepared hydrogel precursor solution to initiate cross-linking. Nitrogen was then blown into the top of the tube, which was quickly sealed and vortexed for 10 s; 900 ml of the hydrogel precursor was pipetted around the lens. The entire mold was sealed inside a petri dish using Parafilm (Parafilm "M," Bemis) and purged with nitrogen. A 365-nm UV (ultraviolet) LED assembly (LZ1-10UV0R-0000, ams OSRAM) with a heat sink (PINLED-4830, Wakefield Thermal) was focused to an ~15-mm spot using a condenser lens (ACL25416U-A, Thorlabs) onto the PDMS lens (fig. S6D-iii). After 1 hour, UV exposure was stopped, and the sealed mold was removed from ice and allowed to rest and continue to polymerize for 23 hours (fig. S6D-iv).

PHySL was then peeled from the silicon wafer and rinsed with DI water to remove dust and unpolymerized precursor solution (fig. S6D-v). The system was then submerged in a 0.33 M hydrazine monohydrate (207942, Sigma-Aldrich) solution for 48 hours to reduce GO into rGO (fig. S6E-i), resulting in a noticeably darker color because of increased photoabsorption (fig. S6E-ii). PHySL was then washed with DI water and submerged in DI water for an additional 24 hours. Last, PHySL was fixed to a 3D-printed or PDMS mount using superglue (fig. S6E-iii,iv).

Mechanical testing

Sample preparation

Sylgard 527 PDMS mixtures in three ratios of part A to part B (1:1, 1:1.3, and 1:1.5) were prepared and then pipetted between two square acrylic sheets separated by 1 mm. The molds were then cured on a warm hot plate (50°C) for 24 hours.

Rectangular samples of PNIPAM-GO and PNIPAM-rGO gels were fabricated in the same fashion as PHySL. Hydrogel precursor solutions were prepared using the same recipe (1 ml of PNIPAM-GO, 60 μl of MBAA stock, 3 mg of potassium persulfate, and 5 μl of *N*,*N*,*N*′,*N*′-tetramethylethylenediamine) and then pipetted between two glass slides separated by 1 mm. The molds were cooled on a chilling platform for 1 hour, then removed, and allowed to continue cross-linking at room temperature for another 23 hours. The resulting gel sheet was submerged in DI water for at least 24 hours to fully swell.

After swelling, the thickness of the gel sheet increased to ~1.5 mm. Rectangular samples 10 mm wide and 50 mm long were cut from the bulk material. To fabricate PNIPAM-rGO samples, PNIPAM-GO samples were submerged in a 0.33 M hydrazine monohydrate solution for 48 hours. In addition, for the NIR actuation experiment, additional samples of PNIPAM-GO and PNIPAM-rGO, 1.5 mm thick, 10 mm wide, and 20 mm long, were cut from the bulk material. The exact dimensions of the materials were measured using calipers.

Samples were then glued to a holding rig using superglue (Loctite 406, Loctite). An overview of the sample preparation process is shown in fig. S18A. The true free length of each individual sample was measured using digital calipers. True stress calculations were performed as detailed in Supplementary Methods.

Frequency sweep

Samples were loaded into a tensile testing device (TA3200-ES, TA Instruments) with a 5-N load cell (SMT1-1.1, Interface Force Measurement Solutions) as shown in fig. S18B. Readings from the load cell were filtered with a 40-Hz low-pass filter. Each sample was subject to 10% strain oscillations with frequencies of 0.1 rad/s up to 100 rad/s to calculate storage and loss modulus (fig. S19A-J). The 10% strain threshold was determined by performing a strain sweep at a fixed frequency of 10 rad/s to determine the linear loading region (fig. S19K). Hydrogel samples were loaded immediately after being removed from a water bath. No additional forms of hydration or environmental modification were provided during the experiment. Specific details about the calculation of elastic modulus, storage modulus, and loss modulus are detailed in Supplementary Methods.

Strain loading

Samples were subject to four levels of strain (25, 50, 75, and 100%) in a linear loading-unloading cyclic test. The strain rate was set to 10 mm/min, and a 5-s dwell was set between loading and unloading. Subsequently, if the sample had not already failed during the loading-unloading process, it was subjected to a 10 mm/s strain until failure.

NIR actuation

A custom water immersion chamber clamp and NIR illumination system were added to the tensile testing setup, as shown in fig. S18 (C and D). NIR light was focused to an ~25-mm spot, with a central radiant flux of 350 mW/cm^2. One sample of each PNIPAM-GO and PNIPAM-rGO was loaded into the tensile testing device and immersion chamber clamp, starting with no water in the chamber. The NIR light was switched on for ~3 hours and then turned off. Two hours after turning the NIR light off, water was added to the immersion chamber to allow for full gel recovery. Because the sample did not change in length, we calculated the nominal stress using the initial cross-sectional area of the gel. However, a decrease in the cross-sectional area was apparent (movie S1).

Microscope imaging

System configuration

PHySL was used in an upright microscope configuration (fig. S7). For NIR control, a 5-W, 850-nm LED (LZ4-40R408-0000, arm OSRAM) was mounted onto a heat sink (DUALLED-5850, Wakefield Thermal) and focused onto an ~35-mm-diameter area using a relay

lens pair consisting of a condenser lens (ACL50832U-B, Thorlabs) and a 100-mm focal length lens (LA1050-B-ML, Thorlabs). The illumination power was measured using a power meter (PM100D with S130C, Thorlabs). At a maximum current of 1 A, the irradiance was 260 mW/cm^2 at the center of PHySL and 150 mW/cm^2 at the edge. Depending on the desired FOV, the tube lens was swapped between a 200-mm focal length (TTL200-A, Thorlabs) lens and a 100-mm focal length (AC508-100-A-ML, Thorlabs) lens. A white LED (MWWHF2, Thorlabs) was used to illuminate the sample. A black and white (PL-D755MU-T, PixelLink) or RGB camera (aca4024-29uc, Basler) was used for black and white or color imaging experiments, respectively. A thermal camera (A600, FLIR) was used to simultaneously monitor the temperature change in PHySL during actuation (Supplementary Methods). Water was infused into the PHySL holding tray at 0.50 ml/hour by a syringe pump (Pump 11 Elite, Harvard Apparatus) to counteract the effects of evaporation. Between experiments, PHySL was removed and fully immersed in water for storage.

Optical target imaging

Custom control code was used to interface with the microscope devices, including LED illumination, cameras, and the motor stage. Timed pulse-width modulation sequences were used to turn the NIR light on and off and modulate its intensity. A mixed optical target was used (R1L1S1N, Thorlabs). Specifically, a 2-mm circular aperture was placed on top of the target, revealing the portion of the optical target imaged while masking out all other features. For target imaging experiments, which were the initial focal shift characterization, power and duration variation, astigmatism, translation, and open-loop focusing experiments, volumetric imaging was performed by scanning the sample using the motor stage. After installing PHySL into the microscope, the height of the sample was adjusted to be in focus. Upon initiating the NIR control sequence, a volumetric scan 8 mm in depth was performed starting from 1 mm above the baseline focus and ending 7 mm further from the baseline focus. Images were captured every 50 μm. Volumetric scans were repeated at intervals of every 5, 15, or 30 min, and each scan took ~90 s to complete. The EFD of PHySL for each volume was identified using the Gaussian derivative method to find the most in-focus plane. ΔEFD for a given time point, t, was calculated as $\Delta\mathrm{EFD}_t = \mathrm{EFD}_t - \mathrm{EFD}_0$, where EFD_0 is the initial measured EFD at the start of the experiment. Additional information about focal shift measurement can be found in Supplementary Methods.

Optical characterization

Three 24-hour cycles of imaging the star target were performed in a continuous sequence. Each cycle consisted of 4 hours of NIR illumination at maximum irradiance (150 to 260 mW/cm^2), followed by 20 hours of no NIR illumination. Image segmentation was performed in MATLAB to facilitate the tracking of lateral shift. To facilitate the analysis of magnification and MTF, a radial unwrapping strategy was used to project the star target into a rectilinear shape pattern. Magnification was calculated by identifying the radius of the concentric rings in the star target. The MTF was calculated by measuring the contrast along linear profiles of the unwrapped image. A 10% contrast threshold was used as the limit of resolvability. Additional information about the processing strategies can be found in Supplementary Methods.

Next, PHySL was illuminated under varying conditions of NIR power and illumination duration, imaging mixed targets consisting of the star or USAF 1951 target. The NIR irradiance was controlled to 100, 75, 50, 37.5, and 25% of the maximum using pulse-width modulation signals. For each of the five power levels, PHySL was illuminated for 4 hours and allowed to recover for 20 hours. Subsequently, the illumination duration was controlled to be 4, 2, 1, 0.5, and 0.25 hours at 100% power. PHySL was illuminated with the corresponding illumination duration and then allowed to recover for at least 12 hours before continuing with the next illumination duration.

Focal length calculation

Under a 4f imaging model, the change in EFD, ΔEFD, is the sum of the change in lens focal length ($\Delta f_{\mathrm{PHySL}}$) because of deformation and the axial movement of the principal planes (Δd)

$$\Delta\mathrm{EFD} = \Delta f_{\mathrm{PHySL}} + \Delta d \tag{1}$$

where the focal length of PHySL, f_{PHySL}, can be calculated as follows

$$M = \frac{f_{\mathrm{tube}}}{f_{\mathrm{PHySL}}} \tag{2}$$

where M is the magnification (calculation detailed in Supplementary Methods), and f_{tube} is the focal length of the tube lens.

Astigmatism imaging

An astigmatic mask consisting of a central hole and two quadrant cutouts was placed on PHySL (fig. S20A). Four hours of NIR illumination at maximum power was followed by 44 hours of recovery. At hour 24, the mask was hand rotated by 90°. After recovery, PHySL was exposed to another 4 hours of NIR illumination, followed by 20 hours of recovery. For this experiment, the x and y EFD values were measured separately (Supplementary Methods). To calculate $\Delta\mathrm{EFD}_x$ and $\Delta\mathrm{EFD}_y$, the initial x EFD was used as the baseline for both x and y; that is, $\Delta\mathrm{EFD}_{x,t} = \mathrm{EFD}_{x,t} - \mathrm{EFD}_{x,0}$ and $\Delta\mathrm{EFD}_{y,t} = \mathrm{EFD}_{y,t} - \mathrm{EFD}_{x,0}$.

Lateral shift imaging

A shift mask consisting of an offset circular aperture was placed on PHySL (fig. S20B). Four hours of NIR illumination at maximum power was followed by 20 hours of recovery. Image segmentation was performed in MATLAB (Supplementary Methods) to facilitate the tracking of lateral shift.

Open-loop focus control

No masks were used for open-loop focus control. PHySL was illuminated with a modified NIR sequence consisting of 4 hours of NIR light at 100% power, 20 min of recovery with NIR off, 10 s of 100% NIR power, and then 4 hours of 35% NIR power to maintain focus at an elevated level. Afterward, PHySL was allowed to recover for 20 hours.

Biological sample imaging

Several microscope slides containing various objects were procured from Carolina Biological Supply. A mask with a 2-mm aperture was placed on top of the slide, masking out objects outside the FOV. Without driving the PHySL lens, images of aphids (30-7930, Carolina), *Dictydium* fungus (29-7328, Carolina), and an ant (30-7986, Carolina) were taken using PHySL in its baseline state.

Next, PHySL was driven to scan through a volumetric sample constructed by stacking three slides. In order, slides containing diatoms (29-5948, Carolina), paramecium (29-6914, Carolina), and pollen (30-4264, Carolina) were stacked on top of each other, forming a volume with a thickness of 2.9 mm. A mask with a 2-mm aperture was placed on top of the slide, masking out objects outside of the FOV. Ground truth images were acquired by imaging the stack with a 10× 0.3–numerical aperture objective (MRH00105, Nikon). Without translating the sample, depth scanning was performed by

driving PHySL with 100% NIR illumination for 4 hours, followed by 20 hours of recovery.

Ambient room imaging

A PHySL-based room-imaging system was constructed according to Fig. 4F. Relative to the 1:1 imaging relay pair, PHySL was positioned to form an infinity-focused system at the maximum focal length. The NIR light source was placed at an angle, and the illumination power was measured to be ~140 to 230 mW/cm^2 from the edge to center. Several objects were placed at varying distances from the imaging system: an integrated circuit (7.5 cm), a flex cable connector (10.3 cm), a playing card displaying the king of hearts (26 cm), a playing card displaying the ace of spades (50.5 cm), and a printout of the Georgia Tech mascot Buzz affixed to a blackboard (203 cm). Depth scanning was performed by illuminating PHySL at 100% NIR power for 4 hours, followed by 20 hours of recovery with no NIR light. Images were normalized, and feature measurement was performed by fitting selected intensity profiles to multiple Gaussian peaks (Supplementary Methods). Ground truth images were acquired using a cell phone camera.

Statistical analysis

Mechanical testing of sample storage and loss modulus was performed on three samples for each material type. Data were analyzed in MATLAB, and each data point is displayed as the mean value of the storage or loss modulus with error bars representing the ±standard deviation across the three samples.

Supplementary Materials

The PDF file includes:
Supplementary Text
Supplementary Methods
Figs. S1 to S24
Tables S1 and S2
References (*106*–*141*)

Other Supplementary Material for this manuscript includes the following:
Movies S1 to S9
Data file S1

REFERENCES AND NOTES

1. W. G. Walter, An imitation of life. *Sci. Am.* **182**, 42–45 (1950).
2. O. Holland, The first biologically inspired robots. *Robotica* **21**, 351–363 (2003).
3. R. Pfeifer, M. Lungarella, F. Iida, Self-organization, embodiment, and biologically inspired robotics. *Science* **318**, 1088–1093 (2007).
4. F. Iida, A. J. Ijspeert, in *Springer Handbook of Robotics*, B. Siciliano, O. Khatib, Eds. (Springer International Publishing, 2016), pp. 2015–2034, 10.1007/978-3-319-32552-1_75.
5. J. Pinskier, D. Howard, From bioinspiration to computer generation: Developments in autonomous soft robot design. *Adv. Intell. Syst.* **4**, 2100086 (2022).
6. M. Cianchetti, C. Laschi, A. Menciassi, P. Dario, Biomedical applications of soft robotics. *Nat. Rev. Mater.* **3**, 143–153 (2018).
7. F. Iida, C. Laschi, Soft robotics: Challenges and perspectives. *Procedia Comput. Sci.* **7**, 99–102 (2011).
8. C. S. X. Ng, M. W. M. Tan, C. Xu, Z. Yang, P. S. Lee, G. Z. Lum, Locomotion of miniature soft robots. *Adv. Mater.* **33**, 2003558 (2021).
9. S. Vee, G. Barclay, N. H. Lents, The glow of the night: The tapetum lucidum as a co-adaptation for the inverted retina. *BioEssays* **44**, e2200003 (2022).
10. W. N. Charman, J. Tucker, The optical system of the goldfish eye. *Vis. Res.* **13**, 1–8 (1973).
11. A. L. Stubbs, C. W. Stubbs, Spectral discrimination in color blind animals via chromatic aberration and pupil shape. *Proc. Natl. Acad. Sci. U.S.A.* **113**, 8206–8211 (2016).
12. M. S. Banks, W. W. Sprague, J. Schmoll, J. A. Q. Parnell, G. D. Love, Why do animal eyes have pupils of different shapes? *Sci. Adv.* **1**, e1500391 (2015).
13. F. Toates, Accommodation function of the human eye. *Physiol. Rev.* **52**, 828–863 (1972).
14. C. Choi, G. J. Lee, S. Chang, Y. M. Song, D.-H. Kim, Inspiration from visual ecology for advancing multifunctional robotic vision systems: Bio-inspired electronic eyes and neuromorphic image sensors. *Adv. Mater.* **36**, e2412252 (2024).
15. Y. Zhou, Z. Sun, Y. Ding, Z. Yuan, X. Qiu, Y. B. Cao, Z. Wan, Z. Long, S. Poddar, S. Kumar, W. Ye, C. L. J. Chan, D. Zhang, B. Ren, Q. Zhang, H.-S. Kwok, M. G. Li, Z. Fan, An ultrawide field-of-view pinhole compound eye using hemispherical nanowire array for robot vision. *Sci. Robot.* **9**, eadi8666 (2024).
16. H. Zhang, S. Lee, Robot bionic vision technologies: A review. *Appl. Sci.* **12**, 7970 (2022).
17. Optotune, "Compact camera modules" (Optotune, 2023); www.optotune.com/compact-camera-modules.
18. D. Quesada-González, A. Merkoçi, Mobile phone-based biosensing: An emerging "diagnostic and communication" technology. *Biosens. Bioelectron.* **92**, 549–562 (2017).
19. Y. Zou, W. Zhang, F. S. Chau, G. Zhou, Miniature adjustable-focus endoscope with a solid electrically tunable lens. *Opt. Express* **23**, 20582–20592 (2015).
20. R. D. g. Daweke, M. Kelp, H. Lehr, O. Mönnich, P. Osiak, "Electromagnetic direct linear drives for medical endoscopes," in *2014 International Conference on Optimization of Electrical and Electronic Equipment (OPTIM)* (IEEE, 2014), pp. 245–251.
21. Y. Zou, F. S. Chau, G. Zhou, Ultra-compact optical zoom endoscope using solid tunable lenses. *Opt. Express* **25**, 20675–20688 (2017).
22. H. Jiang, A. Kanhere, "Biomedical applications of tunable liquid lenses," in *2015 IEEE SENSORS* (IEEE, 2015), pp. 1–4.
23. C. Guo, G. J. Blair, M. Sehgal, F. N. Sangiuliano Jimka, A. Bellafard, A. J. Silva, P. Golshani, M. A. Basso, H. T. Blair, D. Aharoni, Miniscope-LFOV: A large-field-of-view, single-cell-resolution, miniature microscope for wired and wire-free imaging of neural dynamics in freely behaving animals. *Sci. Adv.* **9**, eadg3918 (2023).
24. J. Son, B. Mandracchia, S. Jia, Miniaturized modular-array fluorescence microscopy. *Biomed. Opt. Express* **11**, 7221–7235 (2020).
25. C. Efstathiou, V. M. Draviam, Electrically tunable lenses – Eliminating mechanical axial movements during high-speed 3D live imaging. *J. Cell Sci.* **134**, jcs258650 (2021).
26. S. Liu, C. Zhang, Y. Zhang, T. Wang, A. Zhao, T. Zhou, X. Jia, "Miniaturized spectral imaging for environment surveillance based on UAV platform," in *AOPC 2017: Optical Spectroscopy and Imaging* (SPIE, 2017), vol. 10461, pp. 420–429.
27. Y. Cheng, J. Cao, Y. Zhang, Q. Hao, Review of state-of-the-art artificial compound eye imaging systems. *Bioinspir. Biomim.* **14**, 031002 (2019).
28. K. Askar, B. M. Phillips, Y. Fang, B. Choi, N. Gozubenli, P. Jiang, B. Jiang, Self-assembled self-cleaning broadband anti-reflection coatings. *Colloids Surf. A: Physicochem. Eng. Asp.* **439**, 84–100 (2013).
29. M. S. Kim, M. S. Kim, M. Lee, H. J. Jang, D. H. Kim, S. Chang, M. Kim, H. Cho, J. Kang, C. Choi, J. P. Hong, D. K. Hwang, G. J. Lee, D.-H. Kim, Y. M. Song, Feline eye–inspired artificial vision for enhanced camouflage breaking under diverse light conditions. *Sci. Adv.* **10**, eadp2809 (2024).
30. E. Warrant, in *Encyclopedia of Animal Behavior*, J. C. Choe, Ed. (Academic Press, ed. 2, 2019), pp. 64–79.
31. L. Chen, M. Ghilardi, J. J. C. Busfield, F. Carpi, Electrically tunable lenses: A review. *Front. Robot. AI* **8**, 678046 (2021).
32. D. H. Kim, J. J. Kim, D.-J. Kong, G. J. Lee, Y. M. Song, Bio-inspired tunable optics and photonics: Bridging the gap between nature and technology. *Int. J. Optomechatronics* **18**, 2334293 (2024).
33. S. Xu, H. Ren, S.-T. Wu, Dielectrophoretically tunable optofluidic devices. *J. Phys. D: Appl. Phys.* **46**, 483001 (2013).
34. S. Xu, H. Ren, Y.-J. Lin, M. G. J. Moharam, S.-T. Wu, N. Tabiryan, Adaptive liquid lens actuated by photo-polymer. *Opt. Express* **17**, 17590–17595 (2009).
35. C. Liu, Y. Zheng, R.-Y. Yuan, Z. Jiang, J.-B. Xu, Y.-R. Zhao, X. Wang, X.-W. Li, Y. Xing, Q.-H. Wang, Tunable liquid lenses: Emerging technologies and future perspectives. *Laser Photonics Rev.* **17**, 2300274 (2023).
36. J. Studer, S. Kurmulis, M. Ventura, "White Paper J" (Optotune); https://www.optotune.com/white-paper.
37. N. Hasan, A. Banerjee, H. Kim, C. H. Mastrangelo, Tunable-focus lens for adaptive eyeglasses. *Opt. Express* **25**, 1221–1233 (2017).
38. S.-H. Ahn, Y.-K. Kim, Proposal of human eye's crystalline lens-like variable focusing lens. *Sens. Actuators A: Phys.* **78**, 48–53 (1999).
39. K.-H. Jeong, G. L. Liu, N. Chronis, L. P. Lee, Tunable microdoublet lens array. *Opt. Express* **12**, 2494–2500 (2004).
40. A. Werber, H. Zappe, Tunable microfluidic microlenses. *Appl. Opt.* **44**, 3238–3245 (2005).
41. L. Dong, A. K. Agarwal, D. J. Beebe, H. Jiang, Adaptive liquid microlenses activated by stimuli-responsive hydrogels. *Nature* **442**, 551–554 (2006).
42. X. Zeng, H. Jiang, Tunable liquid microlens actuated by infrared light-responsive hydrogel. *Appl. Phys. Lett.* **93**, 151101 (2008).
43. B. Jin, J.-H. Lee, Z. Zhou, G. Zhang, G.-B. Lee, H. Ren, C. Nah, Adaptive liquid lens driven by elastomer actuator. *Opt. Eng.* **55**, 017107 (2016).
44. W. Zhang, K. Aljasem, H. Zappe, A. Seifert, Completely integrated, thermo-pneumatically tunable microlens. *Opt. Express* **19**, 2347–2362 (2011).

45. A. O. Ashtiani, H. Jiang, Thermally actuated tunable liquid microlens with sub-second response time. *Appl. Phys. Lett.* **103**, 111101 (2013).
46. A. Glasser, Accommodation: Mechanism and measurement. *Ophthalmol. Clin. North Am.* **19**, 1–12 (2006).
47. H. Wei, J. S. Wolffsohn, O. Gomes de Oliveira, L. N. Davies, An artificial lens capsule with a lens radial stretching system mimicking dynamic eye focusing. *Polymers* **13**, 3552 (2021).
48. P. Liebetraut, S. Petsch, J. Liebeskind, H. Zappe, Elastomeric lenses with tunable astigmatism. *Light: Sci. Appl.* **2**, e98 (2013).
49. L. Maffli, S. Rosset, M. Ghilardi, F. Carpi, H. Shea, Ultrafast all-polymer electrically tunable silicone lenses. *Adv. Funct. Mater.* **25**, 1656–1665 (2015).
50. F. Carpi, G. Frediani, S. Turco, D. De Rossi, Bioinspired tunable lens with muscle-like electroactive elastomers. *Adv. Funct. Mater.* **21**, 4152–4158 (2011).
51. M. Ghilardi, H. Boys, P. Török, J. J. C. Busfield, F. Carpi, Smart lenses with electrically tuneable astigmatism. *Sci. Rep.* **9**, 16127 (2019).
52. B. Chen, W. Sun, J. Lu, J. Yang, Y. Chen, J. Zhou, Z. Suo, All-solid ionic eye. *J. Appl. Mech.* **88**, 031016 (2020).
53. S. Nam, S. Yun, J. W. Yoon, S. Park, S. K. Park, S. Mun, B. Park, K. U. Kyung, A robust soft lens for tunable camera application using dielectric elastomer actuators. *Soft Robot.* **5**, 777–782 (2018).
54. B. J. Park, S. Park, M. Choi, S. K. Park, S. Yun, E. Shin, J. W. Yoon, Monolithic focus-tunable lens technology enabled by disk-type dielectric-elastomer actuators. *Sci. Rep.* **10**, 16937 (2020).
55. K. Mishra, D. Van den Ende, F. Mugele, Recent developments in optofluidic lens technology. *Micromachines* **7**, 102 (2016).
56. A. O'Halloran, F. O'Malley, P. McHugh, A review on dielectric elastomer actuators, technology, applications, and challenges. *J. Appl. Phys.* **104**, 071101 (2008).
57. Y. Guo, L. Liu, Y. Liu, J. Leng, Review of dielectric elastomer actuators and their applications in soft robots. *Adv. Intell. Syst.* **3**, 2000282 (2021).
58. C. Tang, B. Du, S. Jiang, Z. Wang, X.-J. Liu, H. Zhao, A review on high-frequency dielectric elastomer actuators: Materials, dynamics, and applications. *Adv. Intell. Syst.* **6**, 2300047 (2024).
59. P. C. Nicolson, J. Vogt, Soft contact lens polymers: An evolution. *Biomaterials* **22**, 3273–3283 (2001).
60. M. Zare, A. Bigham, M. Zare, H. Luo, E. Rezvani Ghomi, S. Ramakrishna, pHEMA: An overview for biomedical applications. *Int. J. Mol. Sci.* **22**, 6376 (2021).
61. M. R. Sarabi, N. Jiang, E. Ozturk, A. K. Yetisen, S. Tasoglu, Biomedical optical fibers. *Lab Chip* **21**, 627–640 (2021).
62. M. S. B. Sadeque, H. K. Chowdhury, M. Rafique, M. A. Durmuş, M. K. Ahmed, M. M. Hasan, A. Erbaş, İ. Sarpkaya, F. Inci, M. Ordu, Hydrogel-integrated optical fiber sensors and their applications: A comprehensive review. *J. Mater. Chem. C* **11**, 9383–9424 (2023).
63. M. Neumann, G. di Marco, D. Iudin, M. Viola, C. F. van Nostrum, B. G. P. van Ravensteijn, T. Vermonden, Stimuli-responsive hydrogels: The dynamic smart biomaterials of tomorrow. *Macromolecules* **56**, 8377–8392 (2023).
64. Z. Li, Y. Zhou, T. Li, J. Zhang, H. Tian, Stimuli-responsive hydrogels: Fabrication and biomedical applications. *VIEW* **3**, 20200112 (2022).
65. S. Chatterjee, P. C.-L. Hui, Review of applications and future prospects of stimuli-responsive hydrogel based on thermo-responsive biopolymers in drug delivery systems. *Polymers* **13**, 2086 (2021).
66. B. Strachota, K. Oleksyuk, A. Strachota, M. Šlouf, Porous hybrid poly(N-isopropylacrylamide) hydrogels with very fast volume response to temperature and pH. *Eur. Polym. J.* **120**, 109213 (2019).
67. A. López-Díaz, A. S. Vázquez, E. Vázquez, Hydrogels in soft robotics: Past, present, and future. *ACS Nano* **18**, 20817–20826 (2024).
68. C. S. Park, Y.-W. Kang, H. Na, J.-Y. Sun, Hydrogels for bioinspired soft robots. *Prog. Polym. Sci.* **150**, 101791 (2024).
69. S. G. Kim, D. Kim, S. Kim, J. Yoon, H. S. Lee, Human-iris-like aperture and sphincter muscle comprising hyperelastic composite hydrogels containing graphene oxide. *Macromol. Mater. Eng.* **304**, 1800560 (2019).
70. M. A. Haq, Y. Su, D. Wang, Mechanical properties of PNIPAM based hydrogels: A review. *Mater. Sci. Eng. C Mater. Biol. Appl.* **70**, 842–855 (2017).
71. M. Kalulu, O. Munyati, O. Oderinde, J. Hu, S. O. Ogungbesan, G. Fu, Robust fabrication of anisotropic bilayer hydrogel embedded with a gradient structure in one layer: Enhanced temperature-responsive bending, shape programmability, and actuator and sensor applications. *J. Appl. Polym. Sci.* **142**, e56707 (2025).
72. M. Li, J. Bae, Tunable swelling and deswelling of temperature-and light-responsive graphene oxide-poly (N-isopropylacrylamide) composite hydrogels. *Polym. Chem.* **11**, 2332–2338 (2020).
73. M. Li, J. Bae, Programmable dual-responsive actuation of single-hydrogel-based bilayer actuators by photothermal and skin layer effects with graphene oxides. *Adv. Mater. Interfaces* **10**, 2300169 (2023).
74. M. Motlagh, R. Geetha, "Physiology, Accommodation" in *StatPearls [Internet]* (StatPearls Publishing, 2022); available from https://www.ncbi.nlm.nih.gov/books/NBK542189/.
75. A. Presland, Applied ocular physiology and anatomy. *Anaesth. Intensive Care Med.* **8**, 379–382 (2007).
76. F. M. Cheng, H. X. Chen, H. D. Li, Recent progress on hydrogel actuators. *J. Mater. Chem. B* **9**, 1762–1780 (2021).
77. R. N. Palchesko, L. Zhang, Y. Sun, A. W. Feinberg, Development of polydimethylsiloxane substrates with tunable elastic modulus to study cell mechanobiology in muscle and nerve. *PLoS One* **7**, e51499 (2012).
78. C. F. Guimarães, L. Gasperini, A. P. Marques, R. L. Reis, The stiffness of living tissues and its implications for tissue engineering. *Nat. Rev. Mater.* **5**, 351–370 (2020).
79. C. Moraes, J. M. Labuz, Y. Shao, J. Fu, S. Takayama, Supersoft lithography: Candy-based fabrication of soft silicone microstructures. *Lab Chip* **15**, 3760–3765 (2015).
80. W. M. Lee, A. Upadhya, P. J. Reece, T. G. Phan, Fabricating low cost and high performance elastomer lenses using hanging droplets. *Biomed. Opt. Express* **5**, 1626–1635 (2014).
81. H. Yuk, T. Zhang, G. A. Parada, X. Liu, X. Zhao, Skin-inspired hydrogel-elastomer hybrids with robust interfaces and functional microstructures. *Nat. Commun.* **7**, 12028 (2016).
82. D. Atchison, *Optics of the Human Eye* (CRC Press, ed. 2, 2023), p. 498.
83. A. Guirao, C. González, M. Redondo, E. Geraghty, S. Norrby, P. Artal, Average optical performance of the human eye as a function of age in a normal population. *Investig. Ophthalmol. Vis. Sci.* **40**, 203–213 (1999).
84. P. Alamdari, O. Nematollahi, A. A. Alemrajabi, Solar energy potentials in Iran: A review. *Renew. Sustain. Energy Rev.* **21**, 778–788 (2013).
85. G. Makrides, B. Zinsser, M. Norton, G. E. Georghiou, M. Schubert, J. H. Werner, Potential of photovoltaic systems in countries with high solar irradiation. *Renew. Sustain. Energy Rev.* **14**, 754–762 (2010).
86. Y. Liu, N. Sun, J. Liu, Z. Wen, X. Sun, S.-T. Lee, B. Sun, Integrating a silicon solar cell with a triboelectric nanogenerator via a mutual electrode for harvesting energy from sunlight and raindrops. *ACS Nano* **12**, 2893–2899 (2018).
87. H. Ying Bai, Q. Li Zhu, H. Lei Cheng, X. Ling Wen, Z. Jian Wang, Q. Zheng, Z. Liang Wu, Muscle-like hydrogels with fast isochoric responses and their applications as soft robots: A minireview. *Mater. Horiz.* **12**, 719–733 (2025).
88. L. Tang, L. Wang, X. Yang, Y. Feng, Y. Li, W. Feng, Poly(*N*-isopropylacrylamide)-based smart hydrogels: Design, properties and applications. *Prog. Mater. Sci.* **115**, 100702 (2021).
89. S. Agarwal, S. Jiang, Y. Chen, Progress in the field of water- and/or temperature-triggered polymer actuators. *Macromol. Mater. Eng.* **304**, 1800548 (2019).
90. L. W. Xia, R. Xie, X. J. Ju, W. Wang, Q. Chen, L. Y. Chu, Nano-structured smart hydrogels with rapid response and high elasticity. *Nat. Commun.* **4**, 2226 (2013).
91. I. H. Kim, S. Choi, J. Lee, J. Jung, J. Yeo, J. T. Kim, S. Ryu, S.-K. Ahn, J. Kang, P. Poulin, Human-muscle-inspired single fibre actuator with reversible percolation. *Nat. Nanotechnol.* **17**, 1198–1205 (2022).
92. Y. Li, J. Luo, G. Xie, D. Zhu, C. Zhao, X. Zhang, M. Liu, Y. Wu, Y. Guo, W. Yu, Recent progress on regulating the LCST of PNIPAM-based thermochromic materials. *ACS Appl. Polym. Mater.* **7**, 1–11 (2024).
93. M. Li, X. Wang, B. Dong, M. Sitti, In-air fast response and high speed jumping and rolling of a light-driven hydrogel actuator. *Nat. Commun.* **11**, 3988 (2020).
94. Q. Liu, G. Nian, C. Yang, S. Qu, Z. Suo, Bonding dissimilar polymer networks in various manufacturing processes. *Nat. Commun.* **9**, 846 (2018).
95. X. Li, Y. Zhao, D. Yan, X. Hou, J. Yang, H. Liu, Dynamic adjustable metalens based on a stretchable substrate with a double-layer metal microstructure. *Appl. Opt.* **62**, 2917–2923 (2023).
96. F. Callewaert, V. Velev, S. Jiang, A. V. Sahakian, P. Kumar, K. Aydin, Inverse-designed stretchable metalens with tunable focal distance. *Appl. Phys. Lett.* **112**, 091102 (2018).
97. P. Lin, Y.-S. Lin, J. Lin, B.-R. Yang, Stretchable metalens with tunable focal length and achromatic characteristics. *Results Phys.* **31**, 105005 (2021).
98. M. Pan, Y. Fu, M. Zheng, H. Chen, Y. Zang, H. Duan, Q. Li, M. Qiu, Y. Hu, Dielectric metalens for miniaturized imaging systems: Progress and challenges. *Light: Sci. Appl.* **11**, 195 (2022).
99. S.-H. Baek, H. Ikoma, D. S. Jeon, Y. Li, W. Heidrich, G. Wetzstein, M. H. Kim, in *2021 IEEE/CVF International Conference on Computer Vision (ICCV)* (IEEE, 2021), pp. 2631–2640.
100. S. Abdollahramezani, O. Hemmatyar, A. Adibi, Meta-optics for spatial optical analog computing. *Nanophotonics* **9**, 4075–4095 (2020).
101. J. Hwang, J. I. Kwon, M. K. Choi, J. A. Lim, C. Choi, Advances and challenges in bio-inspired cameras based on flexible and stretchable optoelectronic devices. *IEEE J. Sel. Top. Quantum Electron.* **30**, 3800911 (2024).
102. D. F. Fernandes, C. Majidi, M. Tavakoli, Digitally printed stretchable electronics: A review. *J. Mater. Chem. C* **7**, 14035–14068 (2019).
103. M. Garrad, G. Soter, A. Conn, H. Hauser, J. Rossiter, A soft matter computer for soft robots. *Sci. Robot.* **4**, eaaw6060 (2019).
104. P. Liu, X.-Y. Kong, L. Jiang, L. Wen, Ion transport in nanofluidics under external fields. *Chem. Soc. Rev.* **53**, 2972–3001 (2024).
105. P. Li, G. Xie, X. Y. Kong, Z. Zhang, K. Xiao, L. Wen, L. Jiang, Light-controlled ion transport through biomimetic DNA-based channels. *Angew. Chem.* **128**, 15866–15870 (2016).
106. S. R. Mishra, J. B. Tracy, Sequential actuation of shape-memory polymers through wavelength-selective photothermal heating of gold nanospheres and nanorods. *ACS Appl. Nano Mater.* **1**, 3063–3067 (2018).

107. M. Andriot, S. Chao, A. Colas, S. Cray, F. De Buyl, J. DeGroot, A. Dupont, T. Easton, J. Garaud, E. Gerlach, "Silicones in industrial applications" in *Inorganic Polymers*, R. D. Jaeger, M. Gleria, Eds. (Nova Science Publishers, 2007).
108. J. M. González-Méijome, M. Lira, A. López-Alemany, J. B. Almeida, M. A. Parafita, M. F. Refojo, Refractive index and equilibrium water content of conventional and silicone hydrogel contact lenses. *Ophthalmic Physiol. Opt.* **26**, 57–64 (2006).
109. K. Ishihara, X. Shi, K. Fukazawa, T. Yamaoka, G. Yao, J. Y. Wu, Biomimetic-engineered silicone hydrogel contact lens materials. *ACS Appl. Bio Mater.* **6**, 3600–3616 (2023).
110. C. Brunette, S. Hsu, W. Macknight, N. S. Schneider, Structural and mechanical properties of polybutadiene-containing polyurethanes. *Polym. Eng. Sci.* **21**, 163–171 (1981).
111. W. B. Ying, Z. Yu, D. H. Kim, K. J. Lee, H. Hu, Y. Liu, Z. Kong, K. Wang, J. Shang, R. Zhang, J. Zhu, R. W. Li, Waterproof, highly tough, and fast self-healing polyurethane for durable electronic skin. *ACS Appl. Mater. Interfaces* **12**, 11072–11083 (2020).
112. H. Ren, S.-T. Wu, Tunable-focus liquid microlens array using dielectrophoretic effect. *Opt. Express* **16**, 2646–2652 (2008).
113. R. H. Spector, "The pupils" in *Clinical Methods: The History, Physical, and Laboratory Examinations*, H. K. Walker, W. D. Hall, J. W. Hurst, Eds. (Butterworths, ed. 3, 1990).
114. J. Wang, Z. Chen, M. Mauk, K.-S. Hong, M. Li, S. Yang, H. H. Bau, Self-actuated, thermo-responsive hydrogel valves for lab on a chip. *Biomed. Microdevices* **7**, 313–322 (2005).
115. L. D'eramo, B. Chollet, M. Leman, E. Martwong, M. Li, H. Geisler, J. Dupire, M. Kerdraon, C. Vergne, F. Monti, Microfluidic actuators based on temperature-responsive hydrogels. *Microsyst. Nanoeng.* **4**, 17069 (2018).
116. R. Takahashi, A. Tanaka, M. Yamaguchi, Biomorphic actuation driven via on-chip buckling of photoresponsive hydrogel films. *Adv. Funct. Mater.* **33**, 2300184 (2023).
117. A. Lendlein, S. Kelch, Shape-memory polymers. *Angew. Chem. Int. Ed. Engl.* **41**, 2034–2057 (2002).
118. R. Luo, J. Wu, N. D. Dinh, C. H. Chen, Gradient porous elastic hydrogels with shape-memory property and anisotropic responses for programmable locomotion. *Adv. Funct. Mater.* **25**, 7272–7279 (2015).
119. D. Wirthl, R. Pichler, M. Drack, G. Kettlguber, R. Moser, R. Gerstmayr, F. Hartmann, E. Bradt, R. Kaltseis, C. M. Siket, S. E. Schausberger, S. Hild, S. Bauer, M. Kaltenbrunner, Instant tough bonding of hydrogels for soft machines and electronics. *Sci. Adv.* **3**, e1700053 (2017).
120. A. Doroudchi, R. Khodambashi, M. Sharifzadeh, D. Li, S. Berman, D. M. Aukes, Tracking control of a miniature 2-DOF manipulator with hydrogel actuators. *IEEE Robot. Autom. Lett.* **6**, 4774–4781 (2021).
121. F. Rieke, D. A. Baylor, Single-photon detection by rod cells of the retina. *Rev. Mod. Phys.* **70**, 1027–1036 (1998).
122. X. Zeng, C. T. Smith, J. C. Gould, C. P. Heise, H. Jiang, Fiber endoscopes utilizing liquid tunable-focus microlenses actuated through infrared light. *J. Microelectromechanical Syst.* **20**, 583–593 (2011).
123. E. W. Hawkes, L. H. Blumenschein, J. D. Greer, A. M. Okamura, A soft robot that navigates its environment through growth. *Sci. Robot.* **2**, eaan3028 (2017).
124. N. F. Lepora, Soft biomimetic optical tactile sensing with the TacTip: A review. *IEEE Sens. J.* **21**, 21131–21143 (2021).
125. J. D. Hubbard, R. Acevedo, K. M. Edwards, A. T. Alsharhan, Z. Wen, J. Landry, K. Wang, S. Schaffer, R. D. Sochol, Fully 3D-printed soft robots with integrated fluidic circuitry. *Sci. Adv.* **7**, eabe5257 (2021).
126. A. P. Singh, M. Tintelott, E. Moussavi, S. Ingebrandt, R. Leupers, X.-T. Vu, F. Merchant, V. Pachauri, Logic operations in fluidics as foundation for embedded biohybrid computation. *Device* **1**, 100220 (2023).
127. M. Wehner, R. L. Truby, D. J. Fitzgerald, B. Mosadegh, G. M. Whitesides, J. A. Lewis, R. J. Wood, An integrated design and fabrication strategy for entirely soft, autonomous robots. *Nature* **536**, 451–455 (2016).
128. J.-M. Geusebroek, F. Cornelissen, A. W. M. Smeulders, H. Geerts, Robust autofocusing in microscopy. *Cytometry* **39**, 1–9 (2000).
129. S. Perez, "Focus measure" (MATLAB Central File Exchange, 2024); www.mathworks.com/matlabcentral/fileexchange/27314-focus-measure.
130. Nikon Instruments Inc., "Modulation transfer function"; www.microscopyu.com/microscopy-basics/modulation-transfer-function.
131. B. Berge, J. Peseux, Variable focal lens controlled by an external voltage: An application of electrowetting. *Eur. Phys. J. E* **3**, 159–163 (2000).
132. A. M. Watson, K. Dease, S. Terrab, C. Roath, J. T. Gopinath, V. M. Bright, Focus-tunable low-power electrowetting lenses with thin parylene films. *Appl. Opt.* **54**, 6224–6229 (2015).
133. C. Li, H. Jiang, Electrowetting-driven variable-focus microlens on flexible surfaces. *Appl. Phys. Lett.* **100**, 231105 (2012).
134. D. Kopp, H. Zappe, Tubular astigmatism-tunable fluidic lens. *Opt. Lett.* **41**, 2735–2738 (2016).
135. S. Seo, Y. Park, C.-J. Park, J. H. Lee, Adjustable tilt angle of liquid microlens with four coplanar electrodes. *IEEE Photonics Technol. Lett.* **28**, 79–82 (2015).
136. M. Xu, D. Xu, H. Ren, I.-S. Yoo, Q.-H. Wang, An adaptive liquid lens with radial interdigitated electrode. *J. Opt.* **16**, 105601 (2014).
137. C.-C. Cheng, C. Alex Chang, J. Andrew Yeh, Variable focus dielectric liquid droplet lens. *Opt. Express* **14**, 4101–4106 (2006).
138. Optotune, "Fast electrically tunable lens EL-3-10" (2020); https://www.optotune.com/el-3-10-lens.
139. J.-K. Lee, K.-W. Park, G.-B. Lim, H.-R. Kim, S.-H. Kong, Variable-focus liquid lens based on a laterally-integrated thermopneumatic actuator. *J. Opt. Soc. Korea* **16**, 22–28 (2012).
140. Proto Supplies, "Servo motor micro SG90"; https://protosupplies.com/product/servo-motor-micro-sg90/.
141. S.-Y. Lee, W.-C. Chen, H.-W. Tung, W. Fang, Microlens with tunable astigmatism. *IEEE Photonics Technol. Lett.* **19**, 1383–1385 (2007).

Acknowledgments: We thank J. Huang, J. Chen, and Y. Hu at the Georgia Institute of Technology for helpful advice on hydrogel fabrication and stimulus-responsive materials. We thank the S. Takayama lab at the Georgia Institute of Technology for the usage of fabrication equipment and the development of the supersoft lithography approach. **Funding:** This research was supported by funding from the following: National Science Foundation Graduate Research Fellowship DGE-2039655 (to C.Z.), National Science Foundation grants 2145235 and 2503686 (to S.J.), National Institutes of Health grant R35GM124846 (to S.J.), and Georgia Institute of Technology Faculty Startup Fund (to S.J.). **Author contributions:** Conceptualization: C.Z. and S.J. Methodology: C.Z. Investigation: C.Z. Visualization: C.Z. Supervision: S.J. Writing—original draft: C.Z. Writing—review and editing: C.Z. and S.J. **Competing interests:** A provisional patent application (63/865,714) for this technology was filed by the Georgia Institute of Technology, with S.J. and C.Z. as coinventors. The authors declare that they have no other competing interests. **Data and materials availability:** All data needed to support the conclusions of this manuscript are included in the main text or Supplementary Materials and accessible via Zenodo: https://doi.org/10.5281/zenodo.16720455.

Submitted 19 February 2025
Accepted 23 September 2025
Published 22 October 2025
10.1126/scirobotics.adw8905

Science Robotics

Bioinspired photoresponsive soft robotic lens

Corey Zheng and Shu Jia

Sci. Robot. **10** (107), eadw8905. DOI: 10.1126/scirobotics.adw8905

Science Robotics (ISSN 2470-9476) is published by the American Association for the Advancement of Science. 1200 New York Avenue NW, Washington, DC 20005. The title *Science Robotics* is a registered trademark of AAAS.